Nanoscale

ROYAL SOCIETY OF CHEMISTRY

PAPER

View Article Online
View Journal | View Issue

Check for updates

Cite this: *Nanoscale*, 2023, **15**, 5486

Lighting up RNA-specific multi-photon and super-resolution imaging using a novel zinc complex†

Zhihui Feng,‡[a] Dongxue Zhang,‡[a,b] Hui Guo,[c] Wenqing Su,[c] Yupeng Tian[c] and Xiaohe Tian *[a]

Received 29th September 2022,
Accepted 11th February 2023

DOI: 10.1039/d2nr05392f

rsc.li/nanoscale

Ribonucleic acid (RNA) probes are critical for understanding the role of RNA dynamics in cellular function but are in short supply due to the lack of optimized imaging systems and excellent fluorescence emission performance. Here, the terpyridine Zn(II) complex (**Zn-T**) with D–π-A configuration and bright aggregation-induced fluorescence emission (AIE) has been fabricated for the selective detection and real-time monitoring of RNA. Impressively, **Zn-T** exhibits a large Stokes shift and three-photon absorption (3PA) activity and responds specifically through hydrophobic interactions with an RNA pocket. The combination of AIE-assisted two-photon fluorescence and stimulated emission depletion (STED) microscopy of **Zn-T** for imaging nuclear RNA has higher spatial resolution and brightness, thus providing an imaging platform for studying RNA-related physiological or pathological processes.

Introduction

Selective detection and imaging of RNA can provide information about its location, dynamics, and function at the cellular level.[1] Over the past few decades, fluorescent probes have become one of the tools for the visualization and long-term tracking of RNA due to their high sensitivity, high selectivity, and non-invasiveness.[2] Unfortunately, traditional organic fluorophores are unstable and mostly planar molecules, which are easily aggregated by π–π stacking, have severe aggregation-induced quenching (ACQ) effects,[3] and are excited by visible light, resulting in limited light penetration, cell photodamage, light scattering, *etc.*[4] The fluorophore with AIE and 3PA activities reported by Tang *et al.* effectively solves the problems faced by traditional fluorophores and they proposed that the strong AIE of the fluorophore contributes to the enhancement of the 3PA signal.[5–7] 3PA in the near-infrared region is one of the most prominent nonlinear optical (NLO) effects and 3PF imaging technology utilizes high-order nonlinear local excitation in the NIR-II region (1000–1700 nm), resulting in a significantly improved penetration depth, spatiotemporal resolution, and signal-to-background ratio (SBR).[8,9] The limitation of Abbe's diffraction makes it difficult for traditional optical fluorescence microscopy to observe the nanoscale RNA structure. The platform is jointly constructed by multi-photon fluorescence, confocal and STED microscopy, which breaks the optical diffraction limit of Abbe's and has an ultra-high resolution, which meets the needs of RNA visualization.[10,11]

The low permeability of cell membranes and nuclear pores, and interference from DNA are inherent barriers to RNA detection and imaging.[12] To date, the only commercially available RNA staining dye is "SYTO RNA-Select", but it inevitably has a fluorescence response to DNA, and the tissue penetration depth and resolution are low, which makes it impossible to accurately detect the fine structure of RNA.[13] To design and synthesize probes that specifically respond to RNA, Peng and coworkers proposed the design concept of a "door-bolt" mechanism. Probes stain DNA mainly by intercalating base pairs or inserting grooves. The major groove of the DNA backbone is 12 Å, the minor groove is 6 Å, and the distance between adjacent base pairs is 3.4 Å. However, the open structure of RNA gives it a spacious pocket relative to DNA, into which only a probe of the right size can fit, providing a scheme for RNA design.[14]

Inspired by the results of the above research and to meet various demands for RNA probes, we designed and synthesized the thiophene terpyridine Zn complex **Zn-T** with a

---

[a] *Huaxi MR Research Centre (HMRRC), Functional and Molecular Imaging Key Laboratory of Sichuan Province, Department of Radiology and National Clinical Research Center for Geriatrics, West China Hospital of Sichuan University, Chengdu 610000, Sichuan Province, China. E-mail: xiaohe.t@wchscu.cn*

[b] *Equipment and Material Department, West China Hospital, Sichuan University, Chengdu, China*

[c] *College of Chemistry and Chemical Engineering, Key Laboratory of Functional Inorganic Materials Chemistry of Anhui Province, Anhui Province Key Laboratory of Chemistry for Inorganic/Organic Hybrid Functionalized Materials, Key Laboratory of Structure and Functional Regulation of Hybrid Materials (Anhui University) Ministry of Education, Institutes of Physical Science and Information Technology, Anhui University, Hefei, 230601, P.R. China*

† Electronic supplementary information (ESI) available. CCDC 2205735. For ESI and crystallographic data in CIF or other electronic format see DOI: **https://doi.org/10.1039/d2nr05392f**

‡ These authors contributed equally to this work.

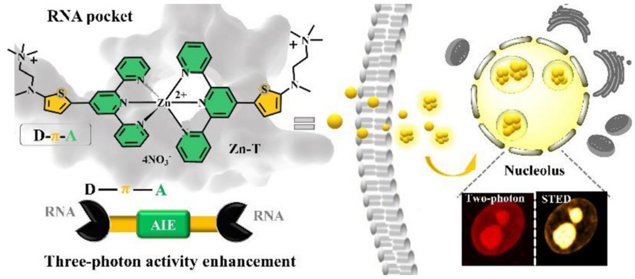

Scheme 1 Probe **Zn-T** with the aggregation-induced nonlinear optical effect can specifically recognize RNA and realize multiphoton confocal and STED imaging of the nucleolus.

D–π-A structure. The hydrophilic quaternary ammonium salt group enhanced the ability of electrostatic interaction with an RNA-negative phosphate skeleton by ensuring good permeability of the cell membrane.[15] **Zn-T** with an octahedral configuration could be specifically inserted in RNA pockets, locking its internal conversion through hydrophobic and π–π interactions to emit strong fluorescence (Table S1†). The NLO activities of **Zn-T** could be obtained using a strong dipolar and long π-conjugated D–π-A structure, which was optimized and enhanced by the introduction of the metal zinc, which is an essential trace element for the human body.[16,17] In addition, the large Stokes shift and high photostability of **Zn-T** facilitate the application of STED microscopy.[18] Notably, **Zn-T** can rapidly pass through cell membranes and nuclear pores to image RNA in the nucleolus. Compared with the commercial dye for RNA (SYTO RNA-Select), **Zn-T** based on AIE activities and 3PA properties exhibits excellent photostability and tissue penetration depth, and visualizes the microstructure of RNA in living cells by STED nanotechnology, providing a new strategy for the design of the RNA probe (Scheme 1).

Results and discussion

Structural features and optical properties

The ligand **DL** and complex **Zn-T** are conjugated systems composed of *N*,*N*,*N*-trimethyl-2-(methylamino) ethan-1-aminium (electron-donor, D), thiophene (π bridge), and terpyridine (electron-acceptor, A) (Fig. 1A). Their synthetic routes are shown in Fig. S1† and their structures were characterized by mass spectrometry and ^{1}H-NMR (Fig. S2–S5†). We obtained a single crystal of the complex **Zn-T** (Fig. S6, CCDC 2205735†), and to deeply understand the optical properties of **DL** and **Zn-T**, the optimized geometry of **DL** was calculated by density functional theory (DFT) at the B3LYP/6-31g(d) level in the gas phase. As shown in Fig. 1B, it was observed that **Zn-T** was more distorted than **DL**; the dihedral angles of the thiophene ring and the adjacent pyridine ring were 16.84° and 7.73°, respectively, and the dihedral angle of the two terpyridine groups of **Zn-T** was 79.74°, which can effectively prevent intermolecular π–π stacking and promote enhancement of the fluorescence intensity of the aggregated state. Furthermore, the C–C bond length between the thiophene ring and the pyridine ring in **Zn-T** was 1.451 Å, which was much lower than that of the ligand **DL** (1.540 Å), indicating that the electron-withdrawing effect of the Zn(II) center improves electron separation and mobility, and thus is conducive to the optimization of NLO activity.[19] The electron density analyses of **DL** and **Zn-T** revealed that their electrons were redistributed from the alkyl chain of the highest occupied molecular orbital (HOMO) to the terpyridine ring of the lowest unoccupied molecular orbital (LUMO), indicating an intramolecular charge transfer (ICT) process (Fig. 1C). Meanwhile, the energy gap of the separated HOMO and LUMO level in **Zn-T** (0.415 eV) was narrower relative to that of **DL** (1.239 eV), which was consistent with the discoloration shift of the absorption and emission spectra. As shown in Fig. 1D, both the absorption and emission peak positions of **Zn-T** showed a redshift relative to those of **DL**, which was attributed to the fact that after the coordination of the terpyridine group with Zn(II), the electron-withdrawing ability of terpyridine was increased, thus improving the intramolecular charge transfer (ICT), laying the foundation for the NLO effect.[20,21]

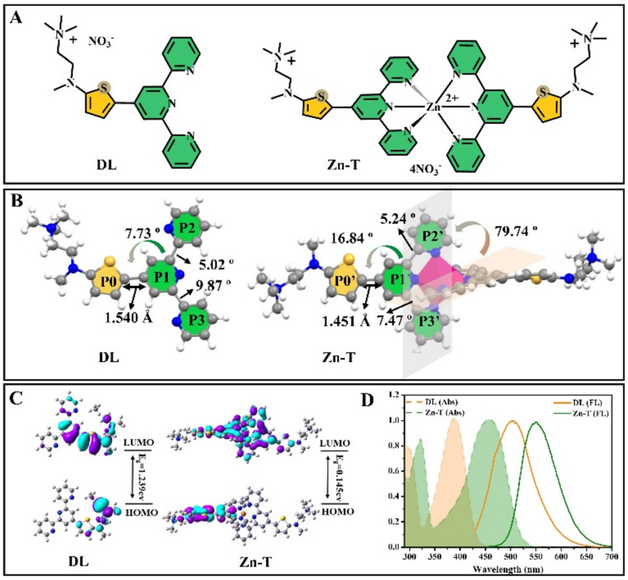

Fig. 1 (A) Chemical structures of ligand **DL** and complex **Zn-T**. (B) Important dihedral angles and bond lengths of **DL** and **Zn-T**, where the structure of **DL** was obtained at B3LYP/6-31g(d) by DFT calculations in the gas phase. (C) Frontier molecular orbitals of the HOMO and LUMO of **DL** and **Zn-T**. (D) Normalized UV-vis absorption and fluorescence emission spectra of **DL** and **Zn-T** (in DMSO, 10 μM).

3PA activities and AIE properties

The above conclusions indicate the potential of **Zn-T** with NLO activities and AIE properties. A detailed study of the solvent coloration effect shows that the Stokes shift of **Zn-T** increases significantly with increasing solvent polarity (Fig. S7 and S8†). As depicted in the resulting Lippert–Mataga plots (Fig. 2A), the slope of **Zn-T** was higher than that of **DL**, demonstrating that

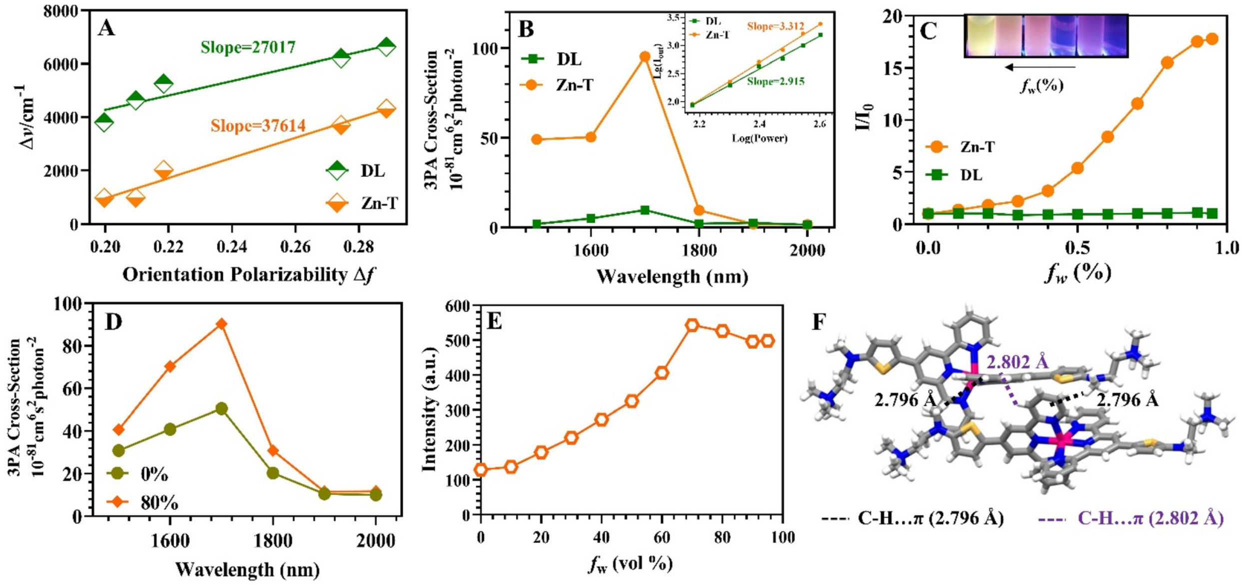

Fig. 2 (A) Lippert–Mataga plot for **DL** and **Zn-T** in various solvents. (B) 3PA cross sections (1500–2000 nm, 500 mW) of **DL** and **Zn-T** in DMSO (c = 1 mM). Inset: ratio of log(I_{out}) to log(power) for **DL** and **Zn-T**. (C) Relative luminescence intensities (I/I_0) of **DL** and **Zn-T** in THF/water mixtures (f_w) of different fractions. Inset: fluorescence images of **Zn-T** with f_w at 0–90%. (D) 3PA cross-sections (1400–2000 nm, 500 mW) of **Zn-T** (c = 0.1 mM) in THF/water mixtures of f_w = 0% and 80%, respectively. (E) Changes in fluorescence intensity of **Zn-T** (10 μM) in different proportions of glycerol/ethanol mixtures (f_w). (F) The intermolecular interaction forces of **Zn-T**.

Zn-T exhibits a more stable polarized excited state and undergoes a stronger ICT process.[22] Owing to the strong push–pull dipolar character of **Zn-T**, interesting NLO properties including 2PA and 3PA activities were detected (Fig. S9 and S10†). The logarithm of the fluorescence intensity of **Zn-T** showed a good linear relationship with the logarithm of the excitation power and the calculated slopes were 1.87 and 3.312, respectively, indicating the existence of the 2PA and 3PA processes. Moreover, the 2PA and 3PA cross-sections of **Zn-T** were 220 GM and 9.81 × 10^{-80} cm^6 per s^2 per photon^2, respectively, which were much higher than ligand **DL** (Fig. 2B and Fig. S11†). The two terpyridine groups in **Zn-T** were perpendicular to each other, which can effectively hinder the intermolecular π–π interaction and show AIE activities. Tetrahydrofuran (THF) and water were used as poor and good solvents for **Zn-T**, and the fluorescence spectra of **DL** and **Zn-T** in water solutions with different THF fraction (f_w) values were measured (Fig. S12†), and the corresponding relative fluorescence intensities were also plotted as shown in Fig. 2C. It can be observed that for **Zn-T**, with the addition of THF, the fluorescence intensity gradually increases, showing the AIE characteristic, which is also reflected in the inset. The 2PA and 3PA cross-section of **Zn-T** in the aggregated state (80%, 76.12 GM, 9.03 × 10^{-80} cm^6 per s^2 per photon^2) was significantly higher than that in the solution state (0%, 16.33 GM, 4.32 × 10^{-80} cm^6 per s^2 per photon^2), indicating that the strong restriction of intramolecular motion (RIM) effect contributes to the enlarged NLO activity (Fig. 2D and S13, 14†). Compared with the reported complexes with AIE activity, **Zn-T** had higher or equivalent 2PA and 3PA cross-sections (Table S3†). In addition, we also studied the emission behavior of complex **Zn-T** in different viscosity environments (Fig. 2E and S15†). In ethanol and glycerol systems, the PL intensity increased with the increasing glycerol ratio (f_w), which further demonstrated the reliability of **Zn-T** in enhancing RIM efficiency at high concentrations or viscosities.[23] Intermolecular interactions further illustrate the large dihedral angle of the **Zn-T** molecule, which prevents the intermolecular π–π stacking, and a large amount of C–H···π in the molecule can activate the AIE activity through RIM (Fig. 2F).[24]

RNA-specific response mechanisms

The large volume of **Zn-T** in octahedral configuration cannot meet the binding conditions of DNA, which lays a foundation for the specific binding of RNA. To further determine the selectivity of **Zn-T** for various species, the fluorescence changes of **Zn-T** in the presence of typical biomolecules (amino acids, ATP, GTP, CTP, UTP, RNA, DNA, and BSA, purchased from Sigma) were measured at pH = 7.3 and it was found that the fluorescence of **Zn-T** was significantly enhanced only in the presence of RNA (Fig. S16†). DNA and RNA had similar structures and even SYTO RNA-Select (a commercial dye for RNA) inevitably had a weak fluorescence response to DNA. However, **Zn-T** had extremely high selectivity for RNA (Fig. S17†). Adding RNA solution to the aqueous solution of **Zn-T** increased the emission intensity by 15.6 times, while adding DNA under the same conditions maintained the emission intensity basically unchanged (Fig. 3A and B). In addition, **Zn-T** showed the following advantages over SYTO RNA-Select (Table S4†): (1) the emission wavelength red shift and background fluorescence interference are reduced; (2) the Stokes

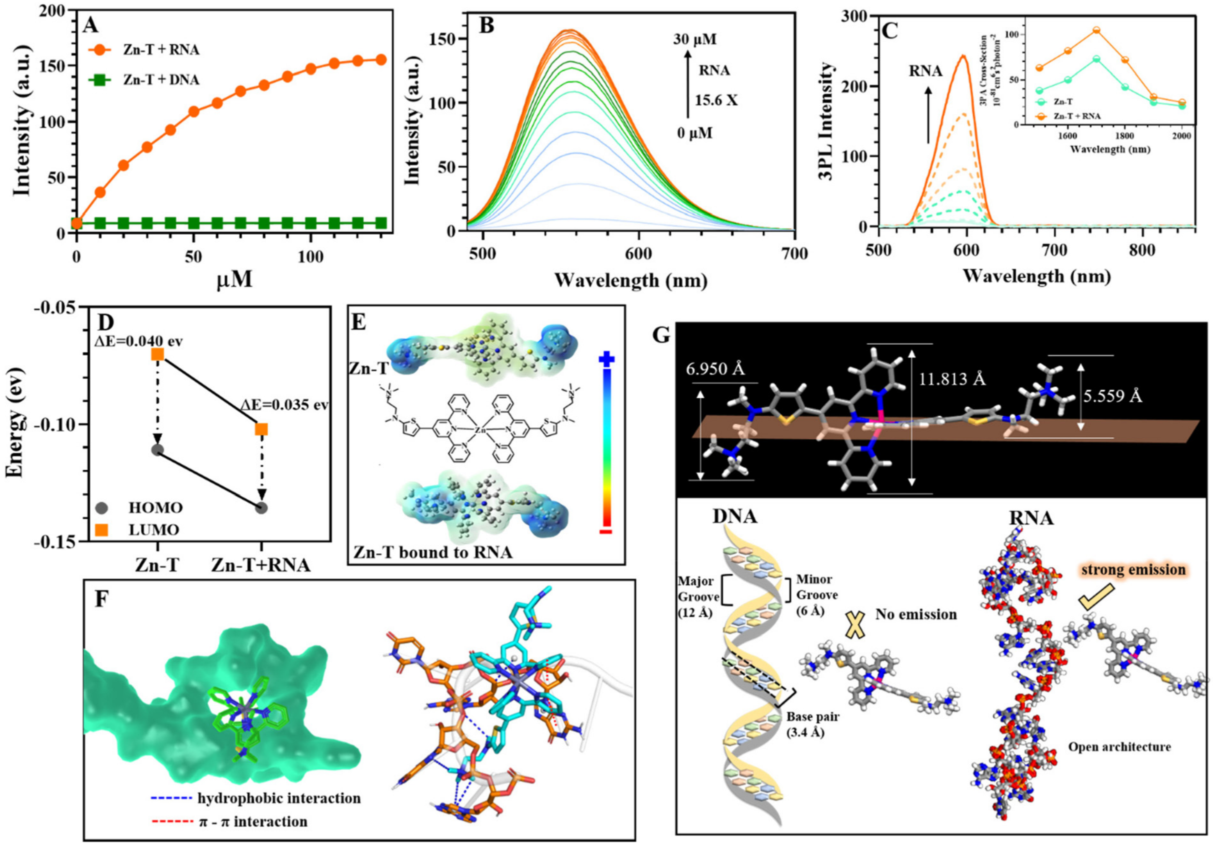

Fig. 3 (A) Fluorescence intensity changes of **Zn-T** (0.01 mM) treated with DNA and RNA at different concentrations (0–30 μM). (B) Fluorescence intensity of **Zn-T** (0.01 mM) *versus* RNA (0–30 μM) content in Tris-HCl buffer (pH = 7.4). Inset: limit plot of RNA titrations. (C) Three-photon fluorescence intensity of **Zn-T** (1 mM) *versus* RNA content in Tris-HCl buffer (pH = 7.4). Inset: 3PA action cross-section changes of **Zn-T** (1 mM) with RNA (30 μM). (D) Energy changes in the HOMO and LUMO orbitals before and after **Zn-T** bound to RNA. (E) Surface electrostatic potential (ESP) before and after **Zn-T** bound to RNA. (F) Cartoon diagram of **Zn-T** binding sites to RNA and a bar diagram of **Zn-T** interactions with bases. (G) The molecular size of **Zn-T** and schematic diagram of the interaction of **Zn-T** with DNA and RNA, respectively.

shift is large (~141 nm), which can effectively eliminate the influence of the excitation spectrum; (3) the quantum yield of **Zn-T** is increased by 23 times before (0.018) and after (0.42) binding with RNA; and (4) high photostability (Fig. S19†). Considering the strong emission of **Zn-T** in the presence of RNA, the 2PA and 3PA activities of **Zn-T** in the presence of RNA were tested (Fig. 3C and Fig. S20†). It was found that with the increase in RNA content, the 2PF and 3PF emissions of **Zn-T** were significantly enhanced, and the 2PA and 3PA cross-sections were also significantly increased. The TD-DFT method was used to calculate the energy changes of the HOMO and LUMO before and after **Zn-T** binding to RNA, and it was found that the energy changes of the HOMO and LUMO and energy gap difference (ΔE) decreased after binding to RNA (Fig. 3D). This may be due to the interaction of **Zn-T** with RNA, which severely restricts the intramolecular motion, thereby reducing the energy loss caused by non-radiative transitions.[25] The electrostatic potential before and after **Zn-T** binding to RNA is shown in Fig. 3E. After binding to RNA, the alkyl region of **Zn-T** was deformed and the potential became negative, indicating that the alkyl site of **Zn-T** might be the site of interaction with RNA. Molecular docking simulation was used to further calculate the existence of π⋯π interactions between **Zn-T** and RNA bases and the hydrophobic interaction between the alkyl region of **Zn-T** and the hydrophobic pocket of RNA (Fig. 3F). The specific binding of **Zn-T** to RNA may be attributed to the molecular size. As shown in Fig. 3G, the heights at both ends of the **Zn-T** molecule were 6.950 Å and 5.559 Å, respectively, and the height of the terpyridine site was 11.813 Å. On account of its excessive size and van der Waals repulsion, **Zn-T** can be inserted neither between DNA base pairs, nor into the major or minor grooves. However, RNA is much more spacious than DNA, and there are many hydrophobic "pockets" in RNA that can accommodate the **Zn-T** molecule. Hydrophobic and π⋯π interactions between **Zn-T** and RNA can lock its internal rotation and emit strong fluorescence.[14]

Intracellular distribution of Zn-T

Encouraged by the fluorescence turn-on response and the superior selectivity of **Zn-T** for RNA, the ability of **Zn-T** to image RNA was examined in HepG2 (human hepatocellular carcinoma) cells acquired from the BeNa culture collection. Excitingly, the viability of HepG2 cells was still up to 68% after 24 h of treatment with 20 μM **Zn-T**, indicating excellent biocompatibility (Fig. S21†). Attributed to the good AIE activity of **Zn-T**, the imaging of cells with different concentrations of **Zn-T** was investigated (Fig. 4A). **Zn-T** can pass through the cell membrane and accumulate in the nucleus, and the imaging intensity was obviously concentration dependent. To determine whether **Zn-T** lighting up the nucleus is closely related to **Zn-T** binding to DNA or RNA, fixed HepG2 cells were treated with DNase or RNase, which specifically catalyzes the hydrolysis of DNA or RNA, respectively (Fig. 4B). After the treatment of HepG2 cells with DNase, the fluorescence signal of the commercially available nuclear dye Hoechst 33342 (DNA staining) disappeared, while the fluorescence signal of SYTO RNA-Select (RNA staining) and **Zn-T** remained basically unchanged. However, after the cells were treated with RNase, the fluorescence signal of Hoechst 33342 remained basically unchanged, while the fluorescence signal of SYTO RNA-Select and **Zn-T** disappeared. Thus, **Zn-T** stains the nucleus by interacting with RNA.[26] HepG2 cells were incubated with **Zn-T** and then examined by transmission electron microscopy (TEM) to determine the aggregation site of **Zn-T** in organelles. HepG2 cells were incubated with osmium tetroxide (OsO_4) as a control experiment to enhance the membrane contrast.[27] In Fig. 4C, cell membrane structures such as mitochondria, plasma membrane, and nuclear membrane can be clearly seen in the cells, whereas, when HepG2 cells were incubated with **Zn-T**, Fig. 4D shows that **Zn-T** was concentrated in the nucleolar region. The TEM study was consistent with the cellular staining of **Zn-T** found by confocal microscopy.

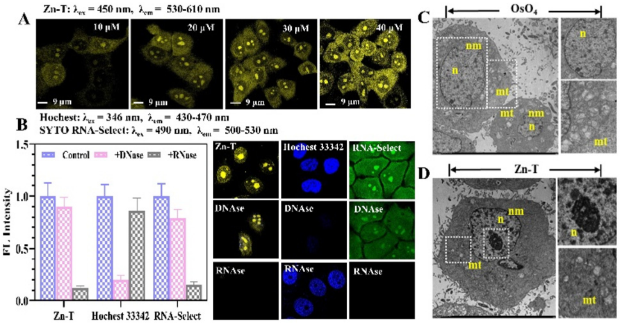

Fig. 4 (A) Concentration-dependent confocal fluorescence imaging of **Zn-T**. (B) Confocal fluorescence images of Hoechst 33342 (commercial DNA probe) and SYTO RNA-Select (commercial RNA probe), and **Zn-T** in RNase- or DNase-treated HepG2-fixed cells. HepG2-fixed cells were incubated with RNase (30 μg mL^{-1}) or DNase (30 μg mL^{-1}) in the medium at 37 °C for 1 hour, followed by staining with Hoechst 33342 for 20 minutes and **Zn-T** (30 μM in 0.02% DMSO) for 20 minutes. (C) TEM images of HepG2 cells incubated with OsO_4 and (D) **Zn-T**, respectively. Abbreviations: n = nucleus, mt = mitochondria, and nm = nuclear membrane.

Cellular localization

The localization of **Zn-T** at the subcellular level in HepG2 cells was assessed using Hochest 33342 (DNA probe) and SYTO RNA-Select (RNA probe). As shown in Fig. 5A, **Zn-T** was mainly distributed in the nucleolar region, while Hochest 33342 was distributed in the nuclear region outside the nucleolus.[28] The

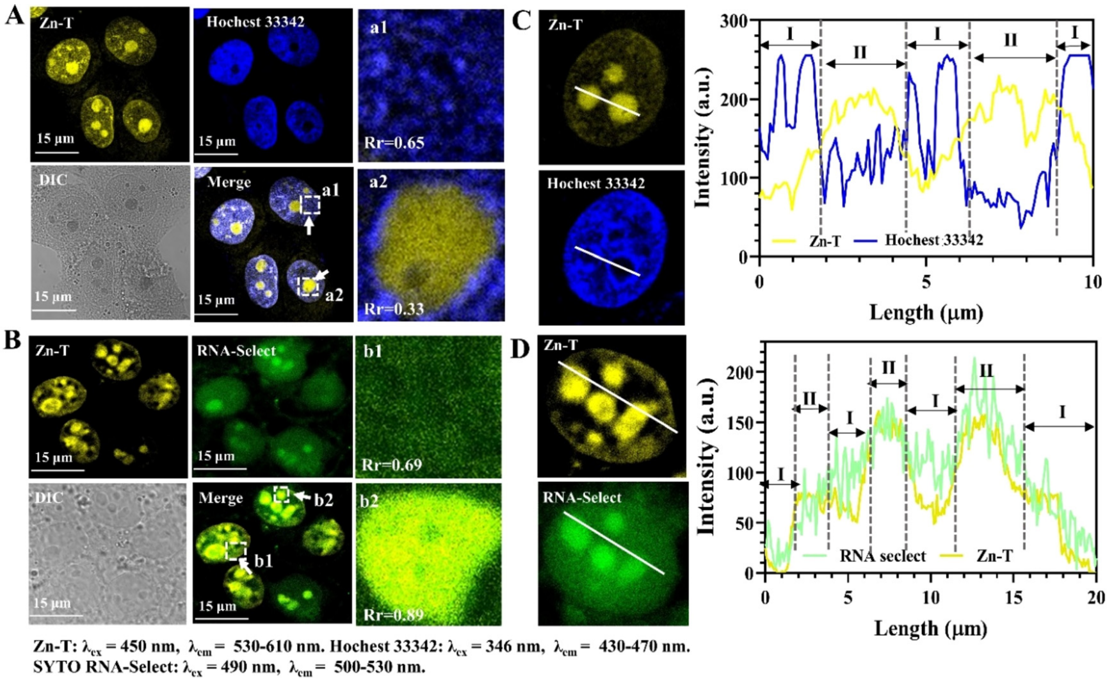

Fig. 5 Confocal fluorescence images of HepG2 cells treated with **Zn-T** and colocalization dye Hochest 33342 (A) and SYTO RNA-Select (B). Comparison of luminescence intensity distributions of Hoechst 33342 (C) and SYTO RNA-Select (D), and **Zn-T** in fixed HepG2 cells. Fluorescence intensity is distributed in the (I) nucleus and (II) nucleolus, where blue, yellow, and red lines represent Hochest 33342, **Zn-T**, and SYTO RNA-Select, respectively.

low degree of overlap between **Zn-T** and Hochest 33342 is also illustrated in the enlarged image (Fig. 5a1 and a2). Fig. 5B showed the co-localization of **Zn-T** with SYTO RNA-Select, with high overlap in the nucleolar region and less overlap in the nuclear region (Fig. 5b1 and b2). As we all know, RNA is mainly distributed in the cytoplasm and nucleolus, while DNA is distributed in the nucleus. This appeal further showed that the specific targeting of **Zn-T** to the nucleolus was attributed to RNA binding. Fig. 5C shows the fluorescence intensity of **Zn-T** and Hochest 33342; the yellow and blue lines are effectively interlaced, and the fluorescence intensity in the nucleus and nucleolus is significantly different, indicating that **Zn-T** can distinguish RNA and DNA in cells. Under the same conditions, the fluorescence intensity contrast of **Zn-T** in the nuclear and nucleolar regions was higher than that of the commercial dye SYTO RNA-Select for RNA, indicating that **Zn-T** had higher RNA selectivity than commercial dyes (Fig. 5D).

Two-photon and STED imaging

The excellent linear and NLO properties of complex **Zn-T** prompted us to evaluate its application in imaging. Compared with one-photon (OP) fluorescence imaging, the intensity of two-photon (TP) imaging is directly proportional to the square of the excitation power, thus TP excitation occurs more strongly in the confined space of the focal plane, thus showing a better signal-to-noise ratio (SNR) in imaging.[29] Fig. 6A and

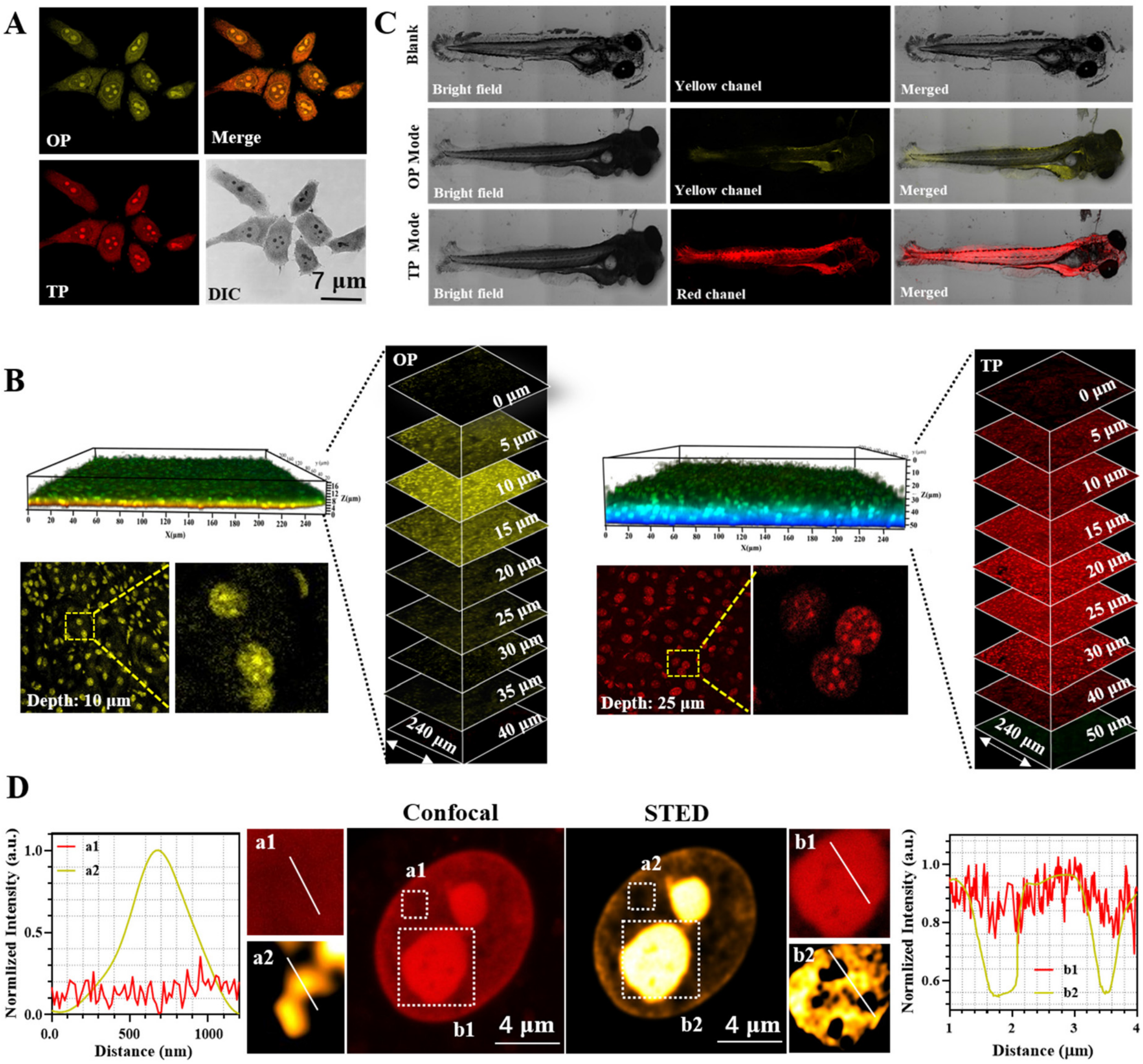

Fig. 6 (A) OP and TP confocal fluorescence imaging of **Zn-T**-incubated HepG2 cells (scale bar: 15 μm). (B) OP (depth: 0–40 μm) and TP (depth: 0–50 μm) 3D fluorescence images of **Zn-T** (30 μM)-soaked liver tissue. OP imaging of liver tissue at a depth of 10 μm and TP imaging at a depth of 25 μm, respectively. (C) OP and TP confocal imaging of the zebrafish incubated with 30 μM **Zn-T** for 1 h. (D) The TP confocal and STED micrograph of living HepG2 cells stained with **Zn-T**, and the amplified parts are nucleolar (b1, b2) and nucleoplasmic region (a1, a2). OP: λ_{ex}, 450 nm; λ_{em}, 550–620 nm. TP: λ_{ex}, 750 nm; λ_{em}, 550–620 nm. STED: donut laser = 595 nm; STED laser power (25 mW). All images were processed using ImageJ and Huygens professional software.

S22† indicate that the TP imaging of **Zn-T** in HepG2 living cells has a higher SNR and better contrast than OP. We further evaluated the utility of **Zn-T** for mouse liver tissue imaging. Sectional OP and TP images of sections labeled with **Zn-T** at depths of 0–50 μm show the distribution of **Zn-T** along the entire depth of the *x*–*y* plane (Fig. 6B). The TP tissue penetration depth (50 μm) of **Zn-T** was about 2.5 times that of OP (20 μm); in addition, at higher magnification, when the penetration depth of OP and TP was 15 μm, 25 μm, respectively, the image still clearly distinguished the staining of nuclei in the tissue. These results demonstrate that **Zn-T** is capable of detecting nuclei in tissues at high depths using TP microscope technology.[30] The zebrafish model showed that in OP and TP modes, **Zn-T** could enter the zebrafish body and emit strong fluorescence, while the fluorescence in the TP mode was stronger, which was beneficial for *in vivo* detection (Fig. 6C). Since **Zn-T** had good photostability, a large Stokes shift and showed emission at near-infrared wavelengths, we were motivated to use such a complex to image live cell nucleus RNA by stimulated emission depletion (STED) microscopy.[31,32] Fig. 6D shows the nuclear structure under STED and TP confocal microscopy, and the selected areas in the images show nucleoplasmic (Fig. 6a1 and a2) and nucleoli (Fig. 6b1 and b2) regions, respectively. Linear complex structures are the predominant form of RNA strands present in chromatin, and TP microscopy cannot obtain more details due to diffraction limitations, while STED microscopy provides tools for in-depth understanding of the ultrastructure of RNA strands.[33] When **Zn-T** stained with live cells was imaged using STED micrographs, high-resolution microscopic images were obtained showing single-celled nucleoli and linearly structured RNAs in the nucleoplasmic region. The normalized fluorescence quantization diagram further illustrates the high resolution and contrast of **Zn-T** in STED microscopy images. This offers the possibility to use such tools in STED microscopy to study the dynamic physiological processes of RNA.

Conclusions

In this work, an AIE probe (**Zn-T**) for RNA imaging was rationally designed and synthesized. Thanks to the D–π-A configuration and the strong electron-withdrawing ability of Zn^{2+}, **Zn-T** exhibits an excellent three-photon absorption cross-section (9.81×10^{-80} cm^6 per s^2 per $photon^2$) under 1700 nm wavelength light excitation. Excellent optical properties provide a solid foundation for biological-specific studies. The positive charge, good water solubility, and appropriate molecular size of **Zn-T** molecules promote their tight binding with RNA and realize the specific selection of RNA, and then target the nucleoli of living cells. On this basis, two-photon and STED super-resolution microscopic images of the nucleus were obtained and the linear RNA was clearly visible. The above results provide a new idea for designing RNA-targeting probes with NLO and super-resolution imaging capabilities.

Author contributions

Zhihui Feng participated in the experimental design, preparation, and characterization of **Zn-T** and wrote this article. Dongxue Zhang: responsible for the cellular visualization of **Zn-T**, including confocal imaging and STED microscopy. Hui Guo and Wenqing Su: conducted tests and analyzed the data. Yupeng Tian: responsible for molecular design, experimental design, and experimental data analysis. Xiaohe Tian: conceptualization, funding acquisition, supervision, project administration, and writing – review & editing.

Conflicts of interest

There are no conflicts to declare.

Acknowledgements

This work was supported by grants from the National Natural Science Foundation of China (32171361 and 21871003), and the National Clinical Research Center for Geriatrics, West China Hospital, Sichuan University (Z2021YY001).

References

1 B. S. Morgan, J. E. Forte and A. E. Hargrove, *Nucleic Acids Res.*, 2018, **46**, 8025–8037.

2 Y. Q. Xia, R. L. Zhang, Z. L. Wang, J. Tian and X. Y. Chen, *Chem. Soc. Rev.*, 2017, **46**, 2824–2843.

3 J. Dai, H. Y. Xue, D. G. Chen, X. D. Lou, F. Xia and S. X. Wang, *Coord. Chem. Rev.*, 2022, **464**, 214552.

4 L. L. Wu, J. H. Liu, P. Li, B. Tang and T. D. James, *Chem. Soc. Rev.*, 2021, **50**, 702–734.

5 W. Qin, N. Alifu, J. W. Y. Lam, Y. H. Cui, H. F. Su, G. D. Liang, J. Qian and B. Z. Tang, *Adv. Mater.*, 2020, **32**, 2000364.

6 Y. L. Wang, X. Han, W. Xi, J. Y. Li, A. W. Roe, P. Lu and J. Qian, *Adv. Healthcare Mater.*, 2017, **6**, 1700685.

7 L. H. Huang, Z. H. Sun, Q. Shen, Z. X. Huang, S. X. Wang, N. D. Yang, G. Q. Li, Q. Wu, W. Wang, L. Li and C. M. Yu, *Chin. Chem. Lett.*, 2022, **33**, 4146–4156.

8 M. B. He, D. Y. Li, Z. Zheng, H. Q. Zhang, T. X. Wu, W. H. Geng, Z. W. Hu, Z. Feng, S. Y. Peng, L. Zhu, W. Xi, D. Zhu, B. Z. Tang and J. Qian, *Nano Today*, 2022, **45**, 101536.

9 Z. R. Xu, Z. J. Zhang, X. Q. Deng, J. G. Li, Y. H. Jiang, W. C. Law, C. B. Yang, W. J. Zhang, X. L. Chen, K. Wang, D. Wang and G. X. Xu, *ACS Nano*, 2022, **16**, 6712–6724.

10 N. T. Urban, M. R. Foreman, S. W. Hell and Y. Sivan, *ACS Photonics*, 2018, **5**, 2574–2583.

11 A. Byrne, C. S. Burke and T. E. Keyes, *Chem. Sci.*, 2016, **7**, 6551–6562.

12 C. Y. Cao, P. Wei, R. H. Li, Y. P. Zhong, X. Li, F. F. Xue, Y. B. Shi and T. Yi, *ACS Sens.*, 2019, **4**, 1409–1416.

13 A. S. Law, L. C. Lee, K. K. Lo and V. W. Yam, *J. Am. Chem. Soc.*, 2021, **143**, 5396–5405.

14 Q. C. Yao, H. D. Li, L. M. Xian, F. Xu, J. Xia, J. L. Fan, J. J. Du, J. Y. Wang and X. J. Peng, *Biomaterials*, 2018, **177**, 78–87.

15 J. Liu, S. L. Zhang, C. H. Zhang, J. Dong, C. Y. Shen, J. Zhu, H. J. Xu, M. K. Fu, G. Q. Yang and X. M. Zhang, *Chem. Commun.*, 2017, **53**, 11476–11479.

16 Z. H. Feng, D. D. Li, M. Z. Zhang, T. Shao, Y. Shen, X. H. Tian, Q. Zhang, S. L. Li, J. Y. Wu and Y. P. Tian, *Chem. Sci.*, 2019, **10**, 7228–7232.

17 Z. J. Fang, Z. Su, W. J. Qin, H. Li, B. Fang, W. Du, Q. Wu, B. Peng, P. Li, H. D. Yu, L. Li and W. Huang, *Chin. Chem. Lett.*, 2020, **31**, 2903–2908.

18 G. N. Liu, J. N. Dai, R. Zhou, G. S. Peng, C. G. Wang, X. Yan, X. T. Jia, X. M. Liu, Y. Gao, L. J. Wang and G. Y. Lu, *Sens. Actuators, B*, 2022, **353**, 131000.

19 Z. H. Feng, T. Zhu, L. K. Wang, T. Yuan, Y. F. Jiang, X. H. Tian, Y. P. Tian and Q. Zhang, *Inorg. Chem.*, 2022, **61**(32), 12652–12661.

20 Y. Yao, H. L. Xu and Z. M. Su, *J. Mater. Chem. C*, 2022, **10**, 886–898.

21 A. Colombo, C. Dragonetti, V. Guerchais, C. Hierlinger, E. Z. Colman and D. Roberto, *Coord. Chem. Rev.*, 2020, **414**, 213293.

22 J. Cao, Q. M. Liu, S. J. Bai, H. C. Wang, X. C. Ren and Y. X. Xu, *ACS Appl. Mater. Interfaces*, 2019, **11**, 29814–29820.

23 L. Li, Z. Lv, Z. W. Man, Z. Z. Xu, Y. L. Wei, H. Geng and H. B. Fu, *Chem. Sci.*, 2021, **12**, 3308–3313.

24 J. Qian, Z. Zhu, A. Qin, W. Qin, L. Chu, F. Cai, H. Zhang, Q. Wu, R. Hu and B. Z. Tang, *Adv. Mater.*, 2015, **27**, 2332–2339.

25 Y. F. Wang, H. Y. Niu, K. Wang, G. Wang, J. W. Liu, T. D. James and H. Zhang, *Anal. Chem.*, 2022, **94**, 7510–7519.

26 A. Saady, E. Varon, A. Jacob, Y. Shav-Tal and B. Fischer, *Dyes Pigm.*, 2020, **174**, 107986.

27 X. H. Tian, Y. Z. Zhu, Q. Zhang, R. L. Zhang, J. Y. Wu and Y. P. Tian, *Chem. Commun.*, 2017, **53**, 7941–7944.

28 Z. Y. Yu, W. H. Luo, J. E. Wang, H. J. Diao, T. Y. Wu, S. T. Zeng, X. C. Chen, Z. S. Huang, J. H. Tan and S. B. Chen, *Sens. Actuators, B*, 2022, **361**, 131730.

29 Z. Zheng, D. Y. Li, Z. Y. Liu, H. Q. Peng, H. H. Y. Sung, R. T. K. Kwok, I. D. Williams, J. W. Y. Lam, J. Qian and B. Z. Tang, *Adv. Mater.*, 2019, **31**, 1904799.

30 J. Chung, H. D. Li, C. S. Lim, H. M. Kim and J. Yoon, *Sens. Actuators, B*, 2020, **322**, 128564.

31 R. Zhou, C. G. Wang, X. H. Liang, F. M. Liu, P. Sun, X. Yan, X. T. Jia, X. M. Liu, Y. Wang and G. Y. Lu, *Theranostics*, 2023, **13**, 95–105.

32 G. W. Jiang, T. B. Ren, E. D'Este, M. Y. Xiong, B. Xiong, K. Johnsson, X. B. Zhang, L. Wang and L. Yuan, *Nat. Commun.*, 2022, **13**, 2264.

33 M. Z. Zhang, W. Du, X. H. Tian, R. L. Zhang, M. Zhao, H. P. Zhou, Y. Q. Ding, L. Li, J. Y. Wu and Y. P. Tian, *J. Mater. Chem. B*, 2018, **6**, 4417.